Journal of Advanced Research in Experimental Fluid Mechanics and Heat Transfer 20, Issue 1 (2025) 68-90

Penerbit Akademia Baru

Journal of Advanced Research in Experimental Fluid Mechanics and Heat Transfer

Journal homepage: http://www.akademiabaru.com/submit/index.php/arefmht
ISSN: 2756-8202

Numerical and Experimental Analysis of Multiphase Flows in Subsea Electric Submersible Pumps

Sharul Sham Dol[1,*], Hasan Hamdan[1], Kamarul Arifin Ahmad[2]

[1] Department of Mechanical Engineering, Faculty of Engineering, Abu Dhabi University, Abu Dhabi, United Arab Emirates
[2] Department of Aerospace Engineering, Faculty of Engineering, Universiti Putra Malaysia, 43400 Serdang, Selangor, Malaysia

ARTICLE INFO

Article history:
Received 20 March 2025
Received in revised form 10 April 2025
Accepted 5 May 2025
Available online 30 June 2025

Keywords:
Electric submersible pump; multiphase flow; gas volume fraction; tip clearance; CFD simulation; high-speed imaging; phase separation

ABSTRACT

Electric Submersible Pumps (ESPs) are widely deployed in oil and gas production, where managing multiphase flow—particularly gas-liquid interactions—remains a key operational challenge. At elevated gas volume fractions (GVFs), gas entrainment can lead to performance degradation, instabilities and reduced hydraulic efficiency. This study combines numerical and experimental methods to assess the effects of GVF and impeller tip clearance on internal ESP flow dynamics. Computational Fluid Dynamics (CFD) simulations were performed using the Eulerian–Eulerian multiphase model with the k-ω SST turbulence model to capture gas-liquid interactions. In parallel, high-speed camera imaging was used in a customized test rig to experimentally visualize transient gas behaviour inside the pump. Numerical results show that at low GVFs, gas follows the liquid streamlines and is well-distributed across the flow domain. As GVF increases, gas accumulates near the impeller tip clearance and diffuser regions, forming recirculating gas pockets that disrupt flow continuity and reduce pressure rise. Larger tip clearance exacerbates gas retention, altering phase separation and further degrading performance. Experimental observations confirm these findings, showing gas clustering around the impeller periphery and extended bubble residence times at higher GVFs. While CFD successfully predicts bulk gas distribution and tip clearance effects, it underrepresents transient gas motions observed experimentally. High-speed footage captured chaotic bubble paths, collapse events and flow recirculation patterns that standard CFD models could not fully resolve—suggesting the need for more advanced turbulence and compressibility modelling. This integrated investigation provides a deeper understanding of ESP gas-handling behaviour under multiphase flow. The results highlight the critical role of tip clearance in gas accumulation, the adverse impact of high GVFs on stability and the importance of refining CFD approaches for improved prediction accuracy. These insights support the development of more efficient and robust ESP systems for gas-laden production environments.

1. Introduction

Electric Submersible Pumps (ESPs) are vital in various industries, including oil and gas, mining, agriculture and water management. These centrifugal pumps are often deployed to lift fluids when

* *Corresponding author.*
E-mail address: sharulshambin.dol@adu.ac.ae (Sharul Sham Dol)

https://doi.org/10.37934/arefmht.20.1.6890

natural pressure is insufficient, such as in oil extraction wells or dewatering applications. In the oil and gas sector, ESPs handle complex operating conditions, including multiphase flows where liquids, gases and solids interact simultaneously [1,2]. This operating environment creates unique challenges such as gas lock, slugging and erosion, which can significantly impact pump performance and longevity.

Multiphase flow within turbomachinery refers to the concurrent movement of two or more immiscible phases, typically liquid, gas and solids. In ESPs, this interaction is further complicated by phenomena like gas lock, where free gas accumulates at the pump's intake or within the stages, leading to performance loss [3-5]. Another common issue, slugging, involves uneven flow conditions with large gas pockets causing mechanical stress and potential pump failure [6,7]. Additionally, the presence of sand or other solids in the fluid can result in erosion and clogging, affecting operational reliability [8].

Designing ESPs for such conditions requires balancing efficiency, stability and durability. A thorough understanding of multiphase flow behaviour and precise performance prediction are essential to achieving this balance. Prior research has focused on evaluating ESP performance under gas-liquid conditions, exploring the effects of gas volume fraction (GVF), cavitation and turbulence on pump behaviour [9-13]. However, gaps remain in understanding how to optimize pump design for high GVF scenarios and accurately model multiphase flow using computational fluid dynamics (CFD).

The goal of this study is to address these gaps by applying advanced CFD techniques to analyse a specific ESP model, the Xylem GDIWA 15T. The study examines flow dynamics under various operating conditions, including the effect of tip clearance, diffuser swirl angle (the angle at which the diffuser blades guide flow into the impeller) and sleeve design on overall performance. Numerical results are validated against experimental data to ensure reliability and accuracy.

CFD simulations have become an indispensable tool in turbomachinery design and analysis, offering insights into complex flow phenomena that are challenging to observe experimentally. For ESPs, CFD enables detailed exploration of flow fields, turbulence dynamics and multiphase interactions. Various modelling approaches, including the Volume of Fluid (VOF) model, mixture model and Eulerian model, have been employed to simulate multiphase flows with different levels of complexity and accuracy [14-18]. These methods allow for studying gas-liquid interfaces, bubble dynamics and turbulent energy dissipation, which are critical for optimizing ESP designs.

This work builds on previous studies, such as those by Bulgarelli *et al.,* [19] and Yang *et al.,* [20], which examined the performance of ESPs under gas-liquid conditions. Specific challenges addressed include the influence of gas volume fraction on head rise, the role of impeller geometry in mitigating performance losses and the onset of surging behaviour. In this context, the reference ESP model is analysed using a combination of experimental validation and CFD simulations to provide a robust assessment of its performance across a wide operating range.

The study also incorporates design modifications, such as adjusting the tip clearance between the impeller and casing and optimizing the diffuser geometry, to evaluate their impact on efficiency and stability. The integration of a sleeve domain, which models the flow stabilization region surrounding the motor housing, further enhances the accuracy of CFD predictions, aligning them closely with experimental observations. These efforts contribute to developing a comprehensive understanding of ESP behaviour under multiphase flow conditions and establishing guidelines for improving future designs.

In addition to addressing gas-liquid interactions, this study investigates the role of tip clearance, which significantly influences ESP performance. Tip clearance, the gap between the impeller blade tip and the casing, affects leakage flows, energy losses and overall pump efficiency [21-24]. Previous studies, such as those by Mansour *et al.,* [25] and Zhu *et al.,* [26], have demonstrated that reducing tip clearance enhances pressure recovery and minimizes energy dissipation. However, excessive reductions can lead to manufacturing challenges and operational risks such as blade erosion or cavitation.

The integration of experimental and numerical analyses forms the core of this study. The experimental setup enables flow visualization and performance measurement, providing a benchmark for validating CFD results. In parallel, numerical simulations using Ansys Fluent explore the pump's performance under a range of operating conditions, including varying flow rates, rotational speeds and gas volume fractions. The combined approach ensures that the findings are both accurate and practically relevant, addressing the limitations of standalone experimental or numerical investigations.

The integration of experimental and numerical analyses forms the core of this study, enabling a comprehensive evaluation of ESP performance under multiphase flow conditions. By combining advanced CFD modelling techniques with experimental validation, this research addresses key challenges like tip clearance effects, geometric optimizations and gas-liquid interactions, providing actionable insights for future ESP designs.

2. Methodology

2.1 Numerical Simulation Framework

2.1.1 Geometry and meshing

The geometry of the ESP under study, Xylem GDIWA 15T, was developed using a combination of CAD modelling and 3D scanning of pump components. The computational domain was divided into two primary regions: the rotating impeller domain and the stationary volute domain. As shown in Figure 1, the geometric assembly was used to extract the fluid domain, where the interaction between water and air bubbles was simulated.

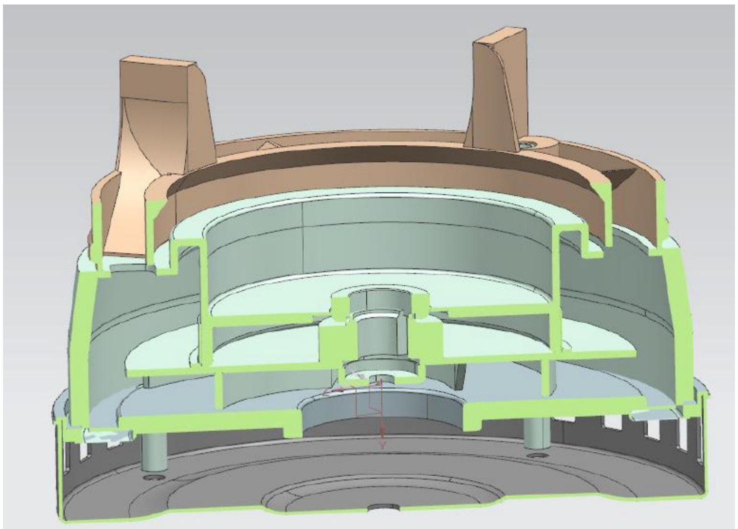

Fig. 1. 3D CAD assembly of the ESP GDIWA 1

The meshing process employed tetrahedral elements, generated using Ansys Meshing software, to balance computational efficiency and accuracy. Inflation layers were added to all walls to capture boundary layer effects, with a first-layer thickness of 3×10^{-5} m^3, resulting in $Y+$ values around 20–30. A sensitivity analysis was conducted with mesh sizes ranging from 500,000 to 5,000,000 elements and a mesh size of 1,600,000 elements was selected as the optimal configuration, providing a good trade-off between accuracy and computational cost (Figure 2).

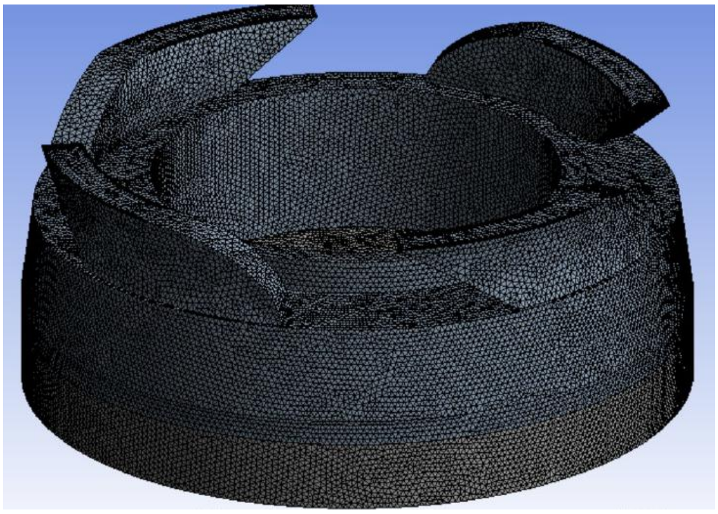

Fig. 2. Selected mesh for characteristic curve CFD study

2.1.2 Governing equations

The simulations used Reynolds-averaged Navier-Stokes (RANS) equations, with turbulence modelled by the k−ω SST model for accurate prediction of separation and shear flows. For multiphase flow, three models were evaluated: Volume of Fluid (VOF), Mixture and Eulerian models [27,28]. The governing equations are as follows:

i. Mass Conservation (Continuity Equation):

$$\frac{\partial \rho}{\partial t} + \nabla \cdot (\rho \vec{v}) = 0 \tag{1}$$

ii. Momentum Conservation:

$$\frac{\partial (\rho \vec{v})}{\partial t} + \nabla \cdot (\rho \vec{v} \vec{v}) = -\nabla p + \nabla \cdot (\mu \nabla \vec{v}) + \rho \vec{g} + \vec{F} \tag{2}$$

where ρ is the fluid density ($\mathrm{Kg/m^3}$), $\vec{\mathrm{v}}$ is velocity ($\mathrm{m/s}$), p is pressure (Pa), μ is dynamic viscosity, $\vec{g}$ is gravitational acceleration ($\mathrm{m/s^2}$) and $\vec{F}$ represents additional forces (e.g., surface tension).

iii. Turbulence Model (k−ω SST):

$$\frac{\partial k}{\partial t} + \nabla \cdot (k \vec{v}) = P_k - \beta^* k \omega + \nabla \cdot [(\nu + \sigma_k \nu_t) \nabla k] \tag{3}$$

$$\frac{\partial \omega}{\partial t} + \nabla \cdot (\omega \vec{v}) = \alpha \frac{k}{\nu_t} P_k - \beta \omega^2 + \nabla \cdot [(\nu + \sigma_\omega \nu_t) \nabla \omega] \tag{4}$$

where k is the turbulent kinetic energy ($\mathrm{m^2/s^2}$), ω is the specific dissipation rate ($\mathrm{s^{-1}}$), P_k is the turbulence production term ($\mathrm{kg/(m \cdot s^3)}$), ν_t is the turbulent viscosity and ν is the kinematic viscosity ($\mathrm{m^2/s}$) and the other empirical coefficients are model-specific.

2.1.3 Multiphase flow models

Volume of Fluid (VOF): Suitable for immiscible phases, where the gas-liquid interface is tracked using the volume fraction equation [29].

$$\frac{\partial \alpha_g}{\partial t} + \nabla \cdot (\alpha_g \vec{v}) = 0 \tag{5}$$

Mixture Model: Simplifies multiphase flow by assuming shared velocity fields [30]:

$$\frac{\partial(\rho_m \vec{v}_m)}{\partial t} + \nabla \cdot (\rho_m \vec{v}_m \vec{v}_m) = -\nabla p + \nabla \cdot (\mu_m \nabla \vec{v}_m) + \rho_m \vec{g} \tag{6}$$

Eulerian Model: Solves separate conservation equations for each phase, ideal for high gas volume fractions. The governing equations include [31]:

i. Mass Conservation:

$$\frac{\partial(\alpha_w \rho_w)}{\partial t} + \nabla \cdot (\alpha_w \rho_w \vec{v}_w) = 0 \tag{7}$$

where α_w is the volume fraction of water (dimensionless), ρ_w is the density of water ($\mathrm{kg/m^3}$) and $\vec{v}_w$ is the velocity of the water phase ($\mathrm{m/s}$).

ii. Momentum Conservation:

$$\frac{\partial(\alpha_w \rho_w \vec{v}_w)}{\partial t} + \nabla \cdot (\alpha_w \rho_w \vec{v}_w \vec{v}_w) = -\alpha_w \nabla p + \nabla \cdot (\tau_w) + \alpha_w \rho_w \vec{g} \tag{8}$$

where p is pressure (Pa), τ_w is the stress tensor (Pa) and $\vec{g}$ is gravitational acceleration ($\mathrm{m/s^2}$).

iii. Volume Fraction Continuity:

$$\alpha_w + \alpha_g = 1 \tag{9}$$

ensuring phase continuity between water and gas (dimensionless).

2.1.4 Boundary conditions and solver settings

The boundary conditions for the computational model were carefully defined to replicate the experimental setup and ensure stable numerical performance (Figure 3). These conditions account for key operational aspects of the ESP, including fluid inflow, outflow and interactions with solid boundaries. By accurately prescribing these parameters, the simulations were able to capture the critical flow phenomena, such as gas-liquid interactions and recirculation zones, that influence ESP performance. Specific boundary conditions were tailored to represent realistic operating scenarios, enabling a robust comparison with experimental results.

i. Inlet: A velocity inlet boundary condition was applied, where the inlet velocity was adjusted to correspond to various flow rates (e.g., 20 L/min to 420 L/min). This approach provides better stability compared to a direct flow rate input. Turbulence intensity at the inlet was set to a default value of 5%, ensuring consistency with the experimental setup.

ii. Outlet: A pressure outlet boundary condition was used, maintaining a constant reference pressure at the outlet to simulate free discharge conditions.
iii. Walls: All solid walls were modelled with a no-slip condition, ensuring accurate simulation of viscous effects. The rotating walls of the impeller were assigned the same rotational speed as the impeller (e.g., 2850 rpm for the reference case), while stationary walls corresponded to the volute and diffuser.
iv. Interface: A sliding mesh interface was employed to couple the rotating impeller domain with the stationary volute domain, allowing accurate simulation of the interaction between these components.

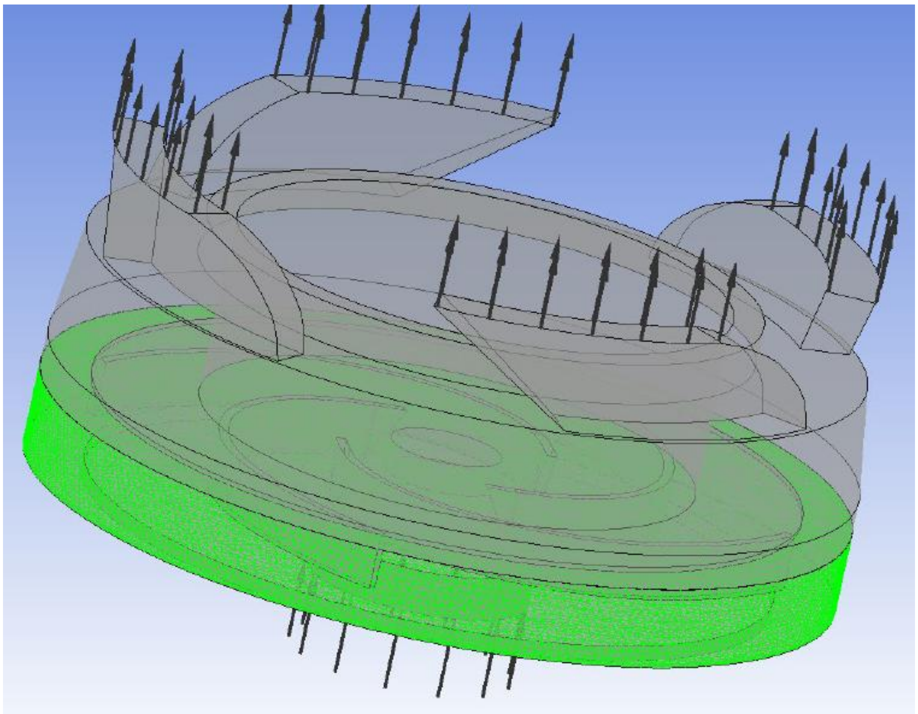

Fig. 3. Representation of boundary conditions, showing inlet velocity, outlet pressure, and wall boundary conditions within the computational domain

The numerical solver settings were designed to ensure stability, convergence and high-fidelity results across all simulations. A pressure-based solver was employed due to its suitability for incompressible multiphase flows. Special attention was given to the discretization schemes, time-stepping methods and turbulence models to capture the intricate flow features, such as cavitation and phase separation, with minimal numerical diffusion. Additionally, pseudo-transient relaxation methods were applied for steady-state cases, while small timestep sizes were adopted for transient simulations to resolve dynamic flow interactions accurately:

i. Solver Type: The pressure-based solver was used, suitable for incompressible and multiphase flow simulations.
ii. Discretization Schemes: Second-order upwind schemes were employed for momentum, turbulence and volume fraction equations to enhance accuracy while maintaining numerical

stability. Gradient reconstruction was performed using the Green-Gauss Node-Based approach.

iii. Turbulence Model: The k−ω SST turbulence model was selected for its robustness in capturing flow separation and shear layer effects, which are critical in ESP performance prediction.
iv. Multiphase Model: Depending on the operating conditions, one of the three multiphase models (VOF, Mixture or Eulerian) was activated to simulate gas-liquid interactions.
v. Time Stepping: For steady-state simulations, pseudo-transient relaxation was applied to improve convergence. Transient simulations were used for scenarios requiring detailed analysis of dynamic behaviour, with a time step size of 1×10^{-4} seconds, ensuring accurate capture of flow interactions.
vi. Convergence Criteria: Residuals for mass, momentum, turbulence and volume fraction equations were monitored and deemed converged when they fell below 10^{-4}. Additionally, global quantities such as head rise and mass flow rate were monitored to ensure physical consistency and convergence.
vii. Computational Resources: Simulations were performed on a multi-core system with GPU acceleration, reducing computation times significantly (e.g., 3–4 hours for steady-state cases and 6–8 hours for transient cases).

2.1.5 Cross-tool verification with ANSYS CFX

To ensure the robustness of the numerical results, cross-verification was performed using Ansys CFX alongside Fluent. The same geometric model, turbulence model (k−ω SST) and boundary conditions were employed in CFX. Key findings from the cross-verification include:

i. Mesh Quality Requirements: CFX required a higher mesh quality for turbomachinery applications to achieve stable convergence. Structured meshing with Turbogrid was used to improve orthogonality and element quality.
ii. Head Rise Validation: Both Fluent and CFX provided similar results for head rise at various flow rates, although Fluent demonstrated better agreement with experimental data.

However, due to the need for additional preprocessing steps and mesh refinement in CFX, Fluent was chosen as the primary solver for subsequent studies. This decision was based on its computational efficiency and the ease of integrating transient multiphase flow models.

2.1.6 Mesh sensitivity analysis

A mesh sensitivity analysis was conducted to ensure numerical accuracy and independence of the results from the mesh resolution. The computational domain was meshed using tetrahedral elements, with inflation layers applied to capture boundary layer effects accurately. The initial layer thickness was set to 3×10^{-5} m, maintaining Y+ values in the range of 20–30.

The sensitivity analysis involved testing mesh sizes ranging from approximately 500,000 to 5,000,000 elements. As shown in Figure 4, key performance metrics such as head rise and pressure distribution were monitored, with negligible variation observed beyond 1.6 million elements. Based on this analysis, a mesh size of approximately 1.6 million elements was selected for all subsequent simulations, balancing computational cost and accuracy.

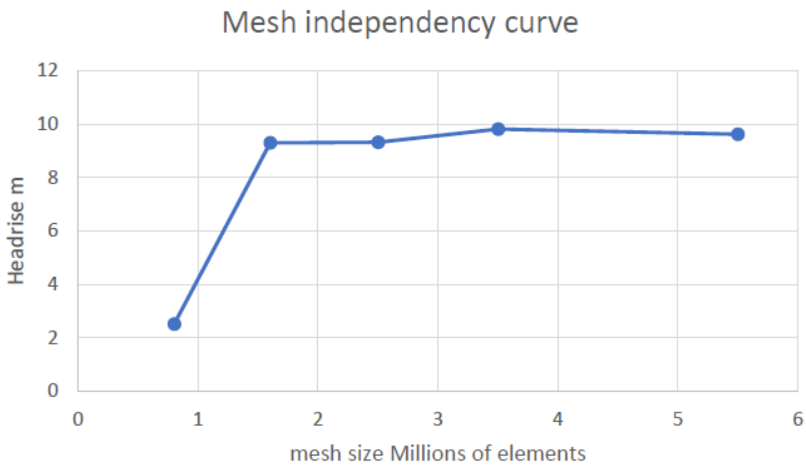

Fig. 4. Mesh independency curve showing the variation of head rise with increasing mesh size. The results indicate negligible changes beyond 1.6 million elements, ensuring mesh-independent solutions

The final mesh configuration ensured adequate resolution of critical regions, such as the impeller blade tips and diffuser vanes, where high velocity gradients and turbulent interactions occur. The results demonstrated that the chosen mesh provided reliable predictions of ESP performance across all operating conditions.

2.2 Experimental Methodology

2.2.1 Overview of the experimental setup

The experimental setup, as illustrated in Figure 5, was designed to evaluate the performance of the Electric Submersible Pump (ESP) under various operating conditions. The system consisted of a 1000 L reservoir, an ESP unit, gas supply for multiphase flow studies and multiple sensors for data acquisition and monitoring.

The reservoir acted as the water source and facilitated recycling of the working fluid throughout the system. The ESP was connected to the reservoir via a closed-loop system, ensuring a controlled environment for assessing pump performance metrics, such as head rise, efficiency and flow characteristics. Gas was introduced into the system to simulate multiphase flow conditions, with the gas-liquid mixture monitored using flow meters and pressure gauges.

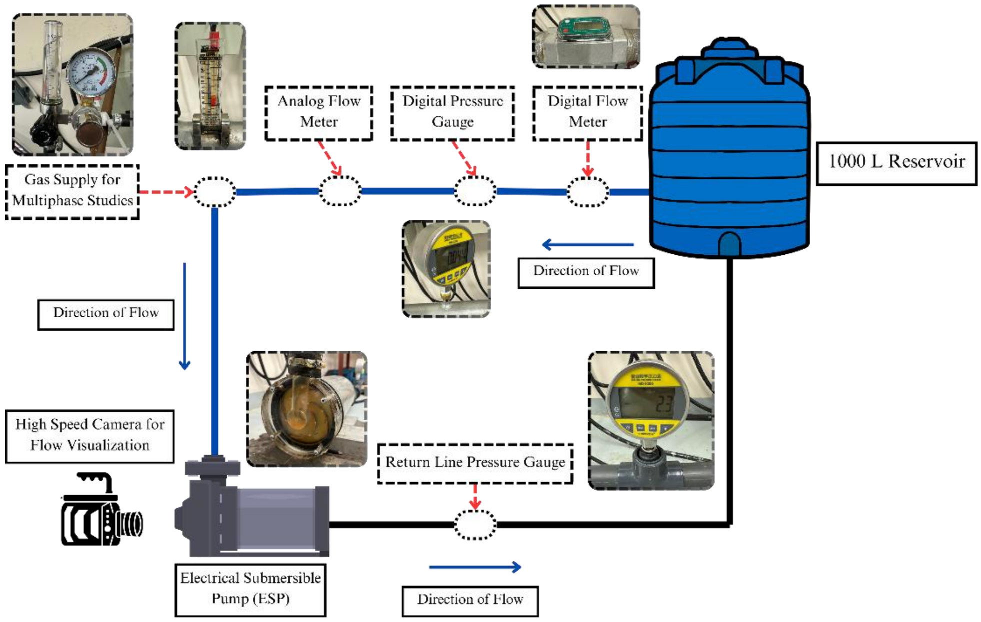

Fig. 5. Experimental setup and system overview

2.2.2 Key components

The experimental setup incorporated several critical components, each contributing to the accuracy, reliability and comprehensiveness of the performance measurements. The Electric Submersible Pump (ESP) used in this study was a multistage centrifugal pump, driven by an electric motor operating at a nominal speed of 2850 rpm. This pump was selected due to its capability to handle high-flow and multiphase applications efficiently, making it well-suited for the operating conditions studied.

A 1000 L reservoir was employed as the primary water supply, enabling closed-loop recycling to ensure consistent fluid flow throughout the experiments. The reservoir's large capacity minimized fluctuations in fluid levels and maintained stable operating conditions during testing. Its role in the setup was vital for providing a reliable water source while reducing waste and allowing for prolonged test durations under varying experimental parameters. To achieve accurate flow measurement and control, both analogue and digital flow meters were utilized. The analogue flow meter was used for initial flow rate adjustments and steady-state monitoring. In contrast, the digital flow meter provided precise real-time flow rate measurements, ensuring the accuracy of performance data. These instruments ensured the precise regulation of flow rates, which ranged between 20 L/min and 420 L/min during testing. Pressure data were collected using a series of digital pressure gauges positioned at strategic locations within the system. These gauges were installed at the ESP inlet and outlet to capture pressure variations across the pump, which are critical for determining head rise and efficiency. Additionally, a return line pressure gauge was included to monitor back pressure in the recirculation loop, enabling a complete understanding of the pressure distribution within the system.

A gas supply system was integrated into the setup to facilitate the introduction of compressed air for multiphase flow studies. The system included a calibrated regulator to adjust the air supply, allowing for precise control of gas volume fractions (GVFs) ranging from 0% to 50%. This capability enabled the simulation of varying multiphase flow conditions, representing real-world operational scenarios.

Finally, a high-speed camera (Figure 6) was deployed near the pump inlet to visualize the flow dynamics under both single-phase and multiphase conditions. The Chronos high-speed camera was used for this purpose, equipped with advanced optics and frame rate capabilities suitable for capturing detailed flow phenomena. This camera operated at two distinct frame rates: 3730 fps for capturing the overall flow field and 6000 fps for detailed analysis of bubble motion and sizing. These high frame rates allowed for the resolution of critical flow phenomena, including bubble formation, coalescence and breakup. The insights gained from these visual recordings complemented the quantitative measurements obtained from the flow meters and pressure gauges, providing a holistic understanding of the phase interactions and dynamic behaviour within the ESP.

Fig. 6. High speed camera utilized to capture detailed flow behaviour at the pump section

2.2.3 Experimental conditions

The performance of the Electric Submersible Pump (ESP) was evaluated under a range of carefully controlled experimental conditions designed to simulate real-world operating scenarios. These conditions included variations in flow rates, rotational speed and gas volume fractions (GVFs), providing a comprehensive assessment of the pump's behaviour under both single-phase and multiphase flow regimes.

Flow rates were varied between 20 L/min and 420 L/min, representing the operational range of the pump. These adjustments were made using the flow meters, with the digital flow meter ensuring precise and accurate measurements. The flow rates were chosen to cover low, medium and high flow scenarios, enabling the analysis of performance metrics across a wide spectrum of operating conditions. The ESP motor was operated at a constant rotational speed of 2850 rpm, consistent with the nominal design speed of the pump. This constant speed ensured uniform energy input, allowing for a reliable comparison of the pump's performance under different test conditions. The chosen speed also corresponded to typical operational conditions for industrial ESPs, ensuring the applicability of the results to practical use cases.

To investigate the effects of multiphase flow, gas volume fractions (GVFs) were varied incrementally between 0% and 50% by regulating the compressed air supply using the calibrated gas regulator. This range of GVFs was selected to represent conditions from pure liquid flow (0% GVF) to challenging multiphase flow scenarios (50% GVF), where significant gas-liquid interactions occur. By studying this range, the experiment captured the transition in pump behaviour as gas content increased, providing insights into the limits of ESP performance under multiphase conditions. During each test, data acquisition was carried out once the system reached steady-state conditions, ensuring that the measurements accurately reflected the pump's performance under stable operating parameters. Measurements from the flow meters and pressure gauges were recorded at 10-second intervals throughout the tests. These data were used to evaluate key performance metrics, including head rise, efficiency and flow characteristics. In addition to quantitative measurements, flow visualization was conducted using a high-speed camera positioned near the pump inlet. The camera captured flow behaviour at two frame rates—3730 fps for an overall view of the flow field and 6000 fps for detailed bubble motion and sizing analysis. These visual observations provided supplementary information on bubble dynamics, coalescence and phase distribution, enhancing the understanding of flow behaviour under varying experimental conditions.

By combining controlled experimental conditions with precise measurements and visual flow analysis, the study was able to thoroughly assess the ESP's performance across a broad range of operating scenarios, both single-phase and multiphase. This comprehensive approach ensured the reliability and applicability of the findings to real-world industrial applications.

3. Results and Discussion

3.1 Numerical Results

The numerical simulation results provide insights into the gas-liquid flow behaviour within the ESP across various operating conditions. The following discussion presents key flow characteristics, including gas distribution, phase separation and flow recirculation, as predicted by CFD.

3.1.1 Gas distribution and entrainment trends

The gas distribution within the ESP varies significantly with rotational speed and gas volume fraction (GVF) at the inlet. At low GVFs, the gas phase is relatively dispersed, following the dominant liquid flow paths. However, as GVF increases, gas pockets start forming in low-pressure regions, leading to flow instability and reduced pump performance.

Figure 7 presents the pressure rise trends for a flow rate of 350 L/min at different rotational speeds and inlet GVFs. The results show that as GVF increases, the pressure rise declines across all speeds. However, at higher rotational speeds, the pump is able to maintain higher head rise values, indicating better gas-handling capability compared to lower-speed operations.

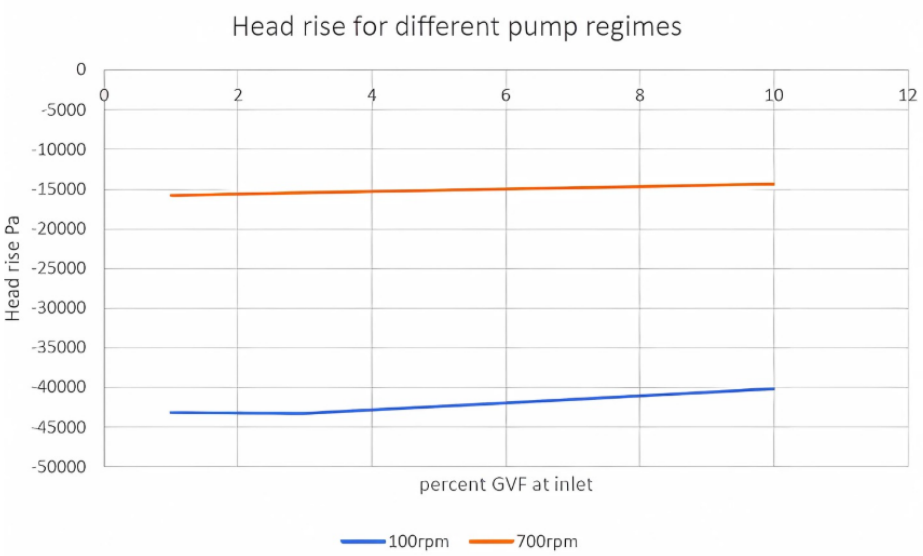

Fig. 7. Pressure rise at 350 L/min for different rotating speeds and inlet GVFs

To better understand the gas movement within the pump, Figure 8 and Figure 9 depict the streamline patterns at 100 rpm (10% GVF) and 700 rpm (3% GVF), respectively. At low speeds, the gas phase remains relatively well-distributed, with minor recirculation zones. However, at higher rotational speeds, gas recirculates more prominently in certain areas, particularly near the blade trailing edges and impeller hub, where flow separation begins to appear

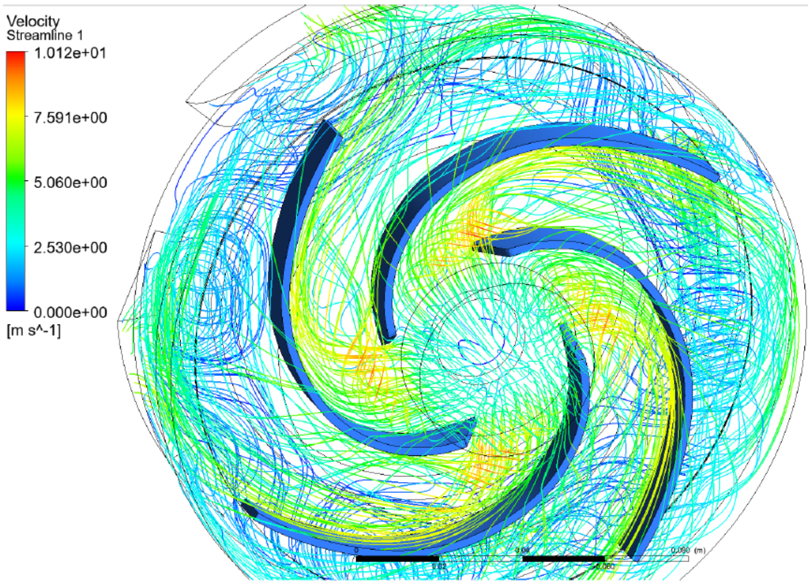

Fig. 8. Flow streamlines at 100 rpm and 10% GVF

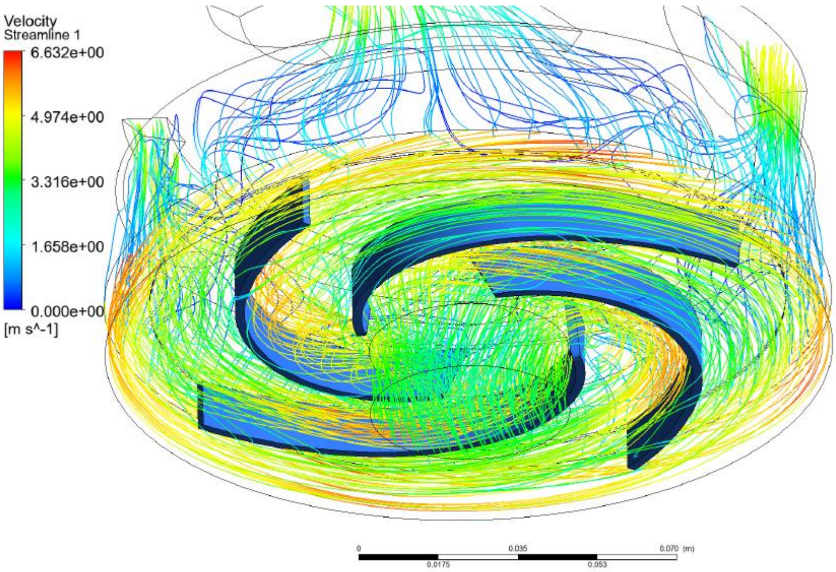

Fig. 9. Flow streamlines at 700 rpm and 3% GVF

3.1.2 Flow recirculation, instability and tip clearance effects

As GVF increases, flow recirculation and instability become more pronounced, particularly around the impeller tip clearance and diffuser regions. The simulations indicate that gas retention zones form near the impeller blade trailing edges, leading to localized reductions in effective liquid momentum and potential performance losses.

Figure 10 presents a visualization of flow streamlines and velocity vectors at 2850 rpm, showing how the gas phase interacts with the liquid as it moves through the pump. While at lower speeds the gas phase remains relatively well-distributed, at higher speeds, recirculating vortices develop near the impeller hub and diffuser vanes, contributing to localized gas entrapment.

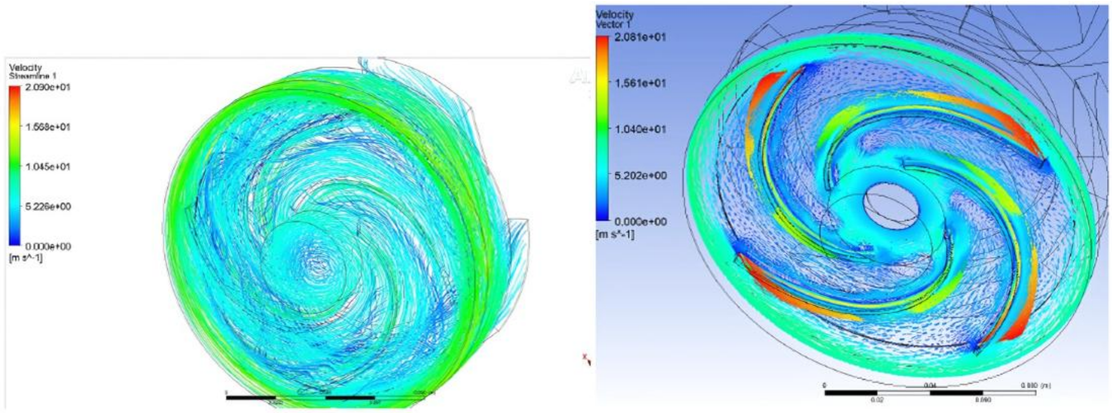

Fig. 10. Flow streamlines and vectors at 2850 rpm

The role of tip clearance is further emphasized in Figure 11, which shows air volume fraction distributions near the impeller tip clearance at 10% GVF. Gas accumulation within this region results in a stagnant gas layer that disrupts the impeller's ability to impart energy to the liquid phase, further contributing to efficiency losses. The formation of these gas pockets is critical, as they can lead to flow separation and unstable pump operation under certain conditions.

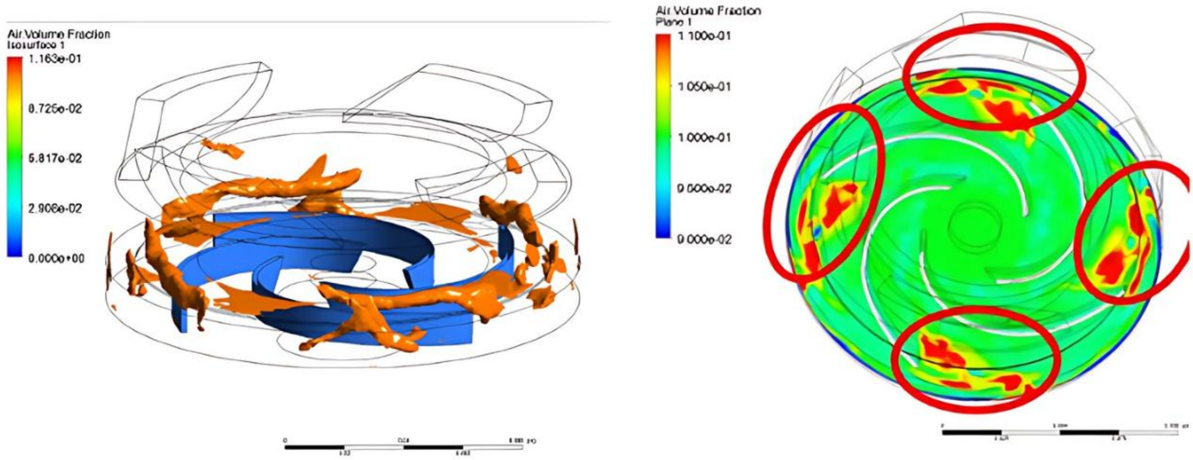

Fig. 11. Air volume fraction near impeller tip clearance at 10% GVF

Additionally, Figure 12 compares the 10% GVF cases at 100 rpm, illustrating how tip clearance influences gas retention. A larger clearance promotes increased gas accumulation, creating a more pronounced blockage effect, while a smaller clearance allows better gas dispersion and more stable operation.

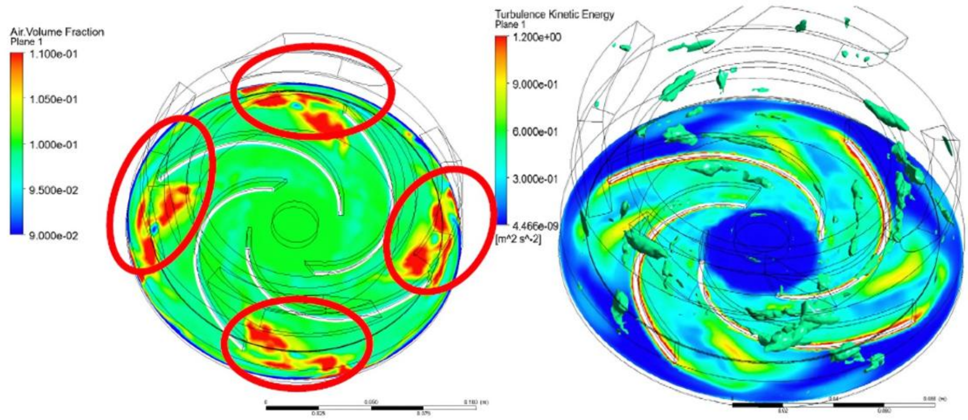

Fig. 12. Comparison of 10% GVF cases at 100 rpm, showing tip clearance influence on gas retention

3.1.3 High GVF effects, phase separation and flow instability

At higher GVFs, gas accumulation and flow instability become more severe, causing significant deviations from expected streamline behaviour. The simulation results indicate that as gas volume fraction increases, large pockets of gas form within the impeller and diffuser regions, leading to flow detachment and a breakdown in the continuous liquid phase.

Figure 13(a) presents an isosurface visualization of the gas volume fraction at 5% GVF, highlighting areas where gas pockets persist. The results show that gas clusters form in low-pressure regions near the blade trailing edges and within the diffuser channels, which aligns with known multiphase flow behaviour in centrifugal pumps.

This effect becomes more pronounced at higher GVFs, as seen in Figure 13(b), where a 7% GVF case shows larger, more unstable gas pockets forming within the pump passage. The increase in gas concentration leads to greater flow resistance, increasing the likelihood of backflow and transient surging behaviour.

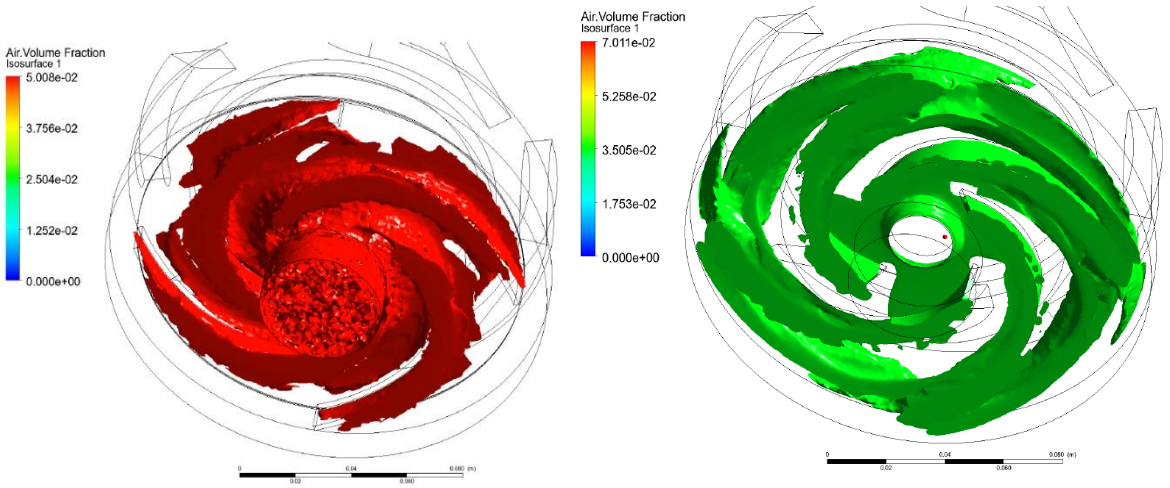

Fig. 13. (a) Isosurface visualization of 5% GVF showing gas pockets and distribution patterns (b) Isosurface at 7% GVF, highlighting gas retention and phase separation

Further illustrating this trend, Figure 14(a) and Figure 14(b) depict flow streamlines and isosurfaces for 20% GVF at an inlet GVF of 7% and a flow rate of 150 L/min. The simulation results confirm that as GVF increases, continuous gas pathways begin to develop, creating conditions where gas is no longer effectively transported with the liquid phase. Instead, the gas phase becomes trapped in recirculating vortices, reducing the overall energy transfer efficiency of the pump.

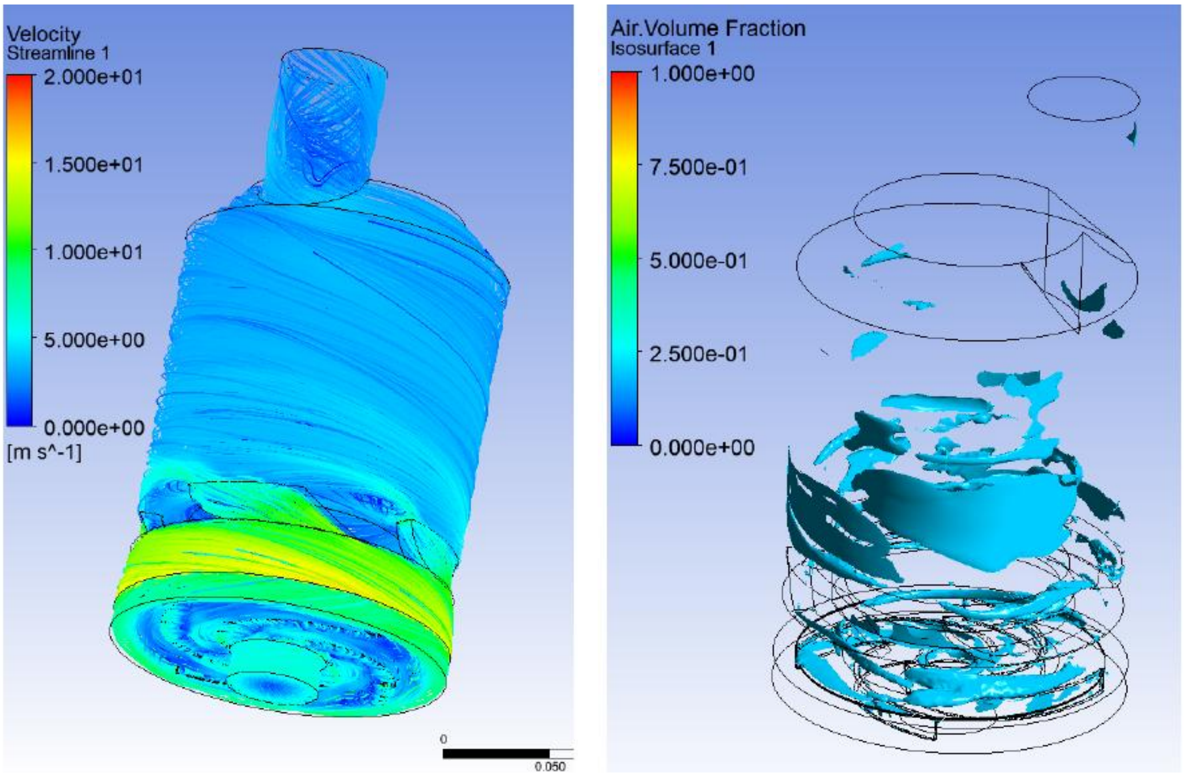

(a) (b)

Fig. 14. (a) Flow streamlines at 20% GVF for 7% GVF inlet, showing gas pathway formation (b) Isosurface at 20% GVF for 7% GVF inlet, 150 L/min, showing recirculating gas structures

3.2 Experimental Observations from High-Speed Camera

The high-speed camera images provide direct visual evidence of the multiphase flow behaviour within the ESP, complementing the numerical findings. These observations offer insight into bubble formation, gas clustering, phase separation and flow instability, allowing for a detailed comparison with CFD predictions. It should be noted that in the notations, green arrows are used to represent liquid-gas flow on the inner side of the impeller towards the tip, while red arrows are used to highlight the flow direction of the outermost liquid-gas mixture (close and near the impeller tip clearance region).

3.2.1 Gas distribution and initial bubble formation

At lower rotational speeds, gas entrainment within the liquid phase follows a relatively uniform distribution, with bubbles being carried along the primary flow paths. Figure 15 presents high-speed footage at 500 rpm, showing early-stage gas distribution and bubble formation. The captured bubbles exhibit dispersion along the impeller channels before migrating toward the tip clearance region. This behaviour aligns well with the streamline patterns observed in Figure 8 and Figure 9, which depict the expected motion of the gas phase under similar conditions.

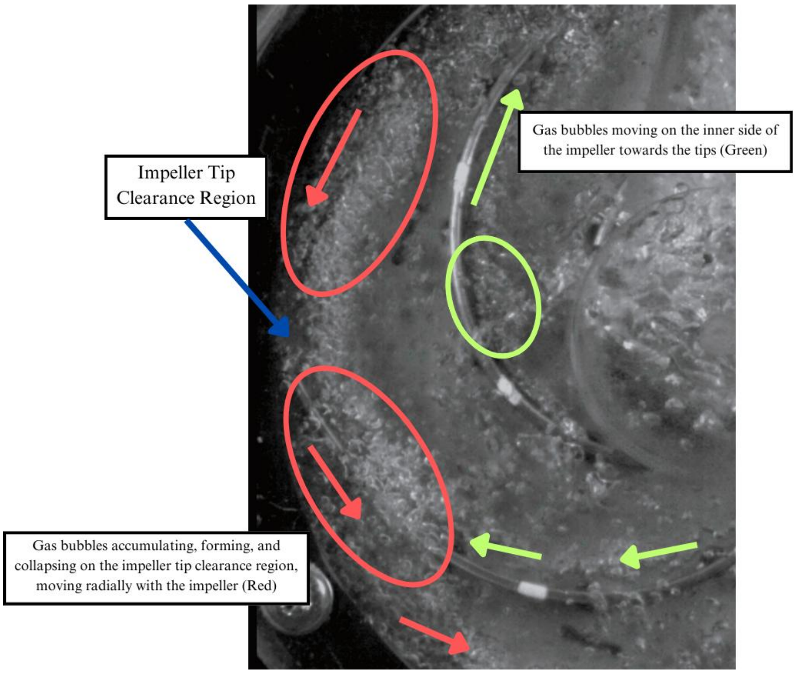

Fig. 15. Gas distribution and bubble formation at 500 rpm, capturing initial entrainment patterns

As the impeller blades continue accelerating the flow, the gas experiences shear forces that promote coalescence and phase separation. Figure 16 highlights this effect at 750 rpm, where bubbles begin to cluster more prominently. These clusters resemble the gas accumulation regions predicted in Figure 11, confirming that blade-induced pressure gradients contribute to localized phase separation and retention zones.

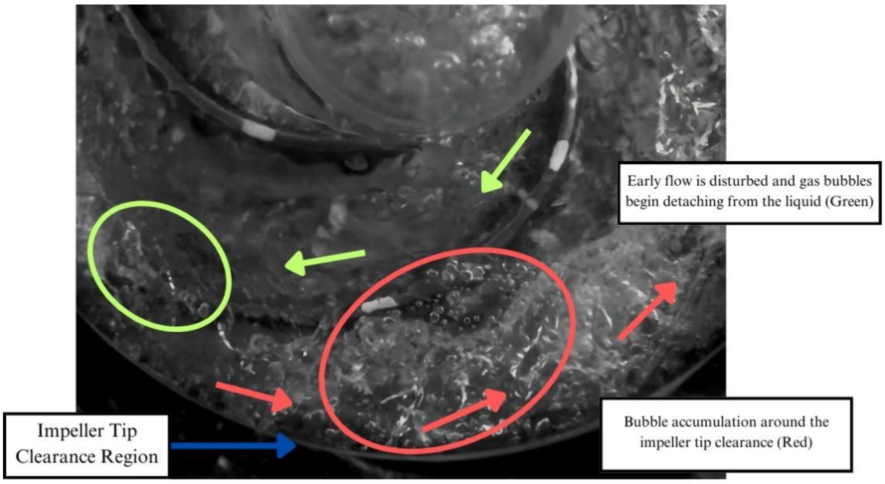

Fig. 16. Phase separation and gas cluster formation at 750 rpm, indicating early-stage recirculation

3.2.2 Gas recirculation, flow instability and phase separation

As rotational speed increases, the gas phase exhibits more complex motion, including recirculation zones, flow detachment and phase separation. High-speed footage at 750 rpm reveals that gas does not simply follow a direct outward path but instead becomes trapped in specific recirculating regions, particularly near the impeller tip clearance and hub.

Figure 17(a) and (b) illustrate this effect, showing snapshots taken at ~0:20s and ~0:30 from high-speed footage at 750 rpm (6k fps). These images highlight how gas separates from the liquid phase and forms distinct paths along the impeller blade passages. Compared to the CFD-predicted streamline behaviour in Figures 10 and 11, the experimental results confirm that gas clustering occurs near the blade trailing edges and tip clearance region, supporting the simulation's prediction of retention zones.

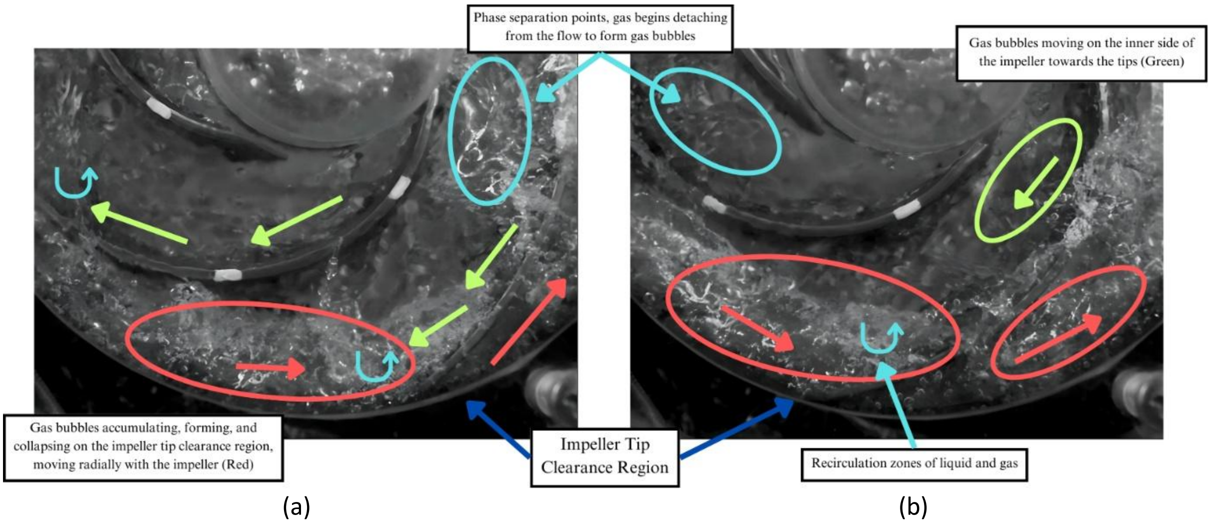

Fig. 17. (a) Phase separation and gas path tracking at 750 rpm, captured at ~0:20s (b) Phase separation and gas path tracking at 750 rpm, captured at ~0:30

Additionally, at 1250 rpm, gas retention becomes even more apparent. Figure 18 captures air accumulation near the impeller tip clearance, showing how gas pockets remain trapped rather than exiting smoothly. This observation aligns with the numerical results in Figure 12, which demonstrated that tip clearance effects contribute to localized phase separation and instability.

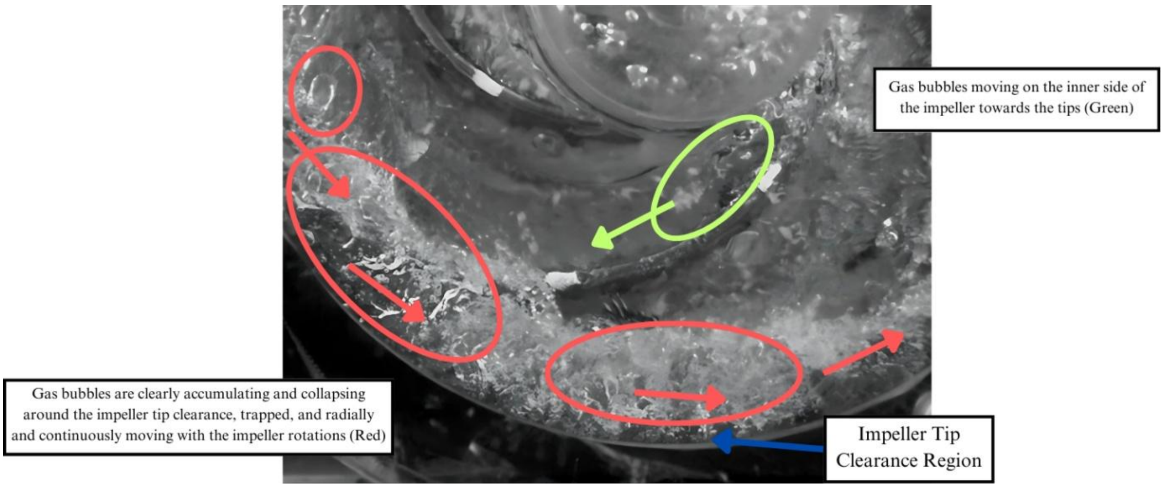

Fig. 18. Air accumulation around impeller tip clearance at 1250 rpm, showing recirculating gas pockets

3.2.3 High GVF effects, surging behaviour and bubble collapse

At higher GVFs, the experimental observations show increasing flow instability, gas clustering and transient surging effects, similar to trends predicted in the simulations. The high-speed footage at 1750 rpm reveals that gas no longer moves uniformly with the liquid phase; instead, it forms large, unstable structures that fluctuate in position and size due to local pressure variations.

Figure 19 captures these effects at ~0:40s from 6k fps footage at 1750 rpm, showing the presence of gas accumulation and chaotic flow behaviour. This behaviour closely aligns with the numerical findings in Figure 13(b), where CFD predicted that at high GVFs, gas pockets become more dominant, leading to unsteady flow fields and increased turbulence intensity.

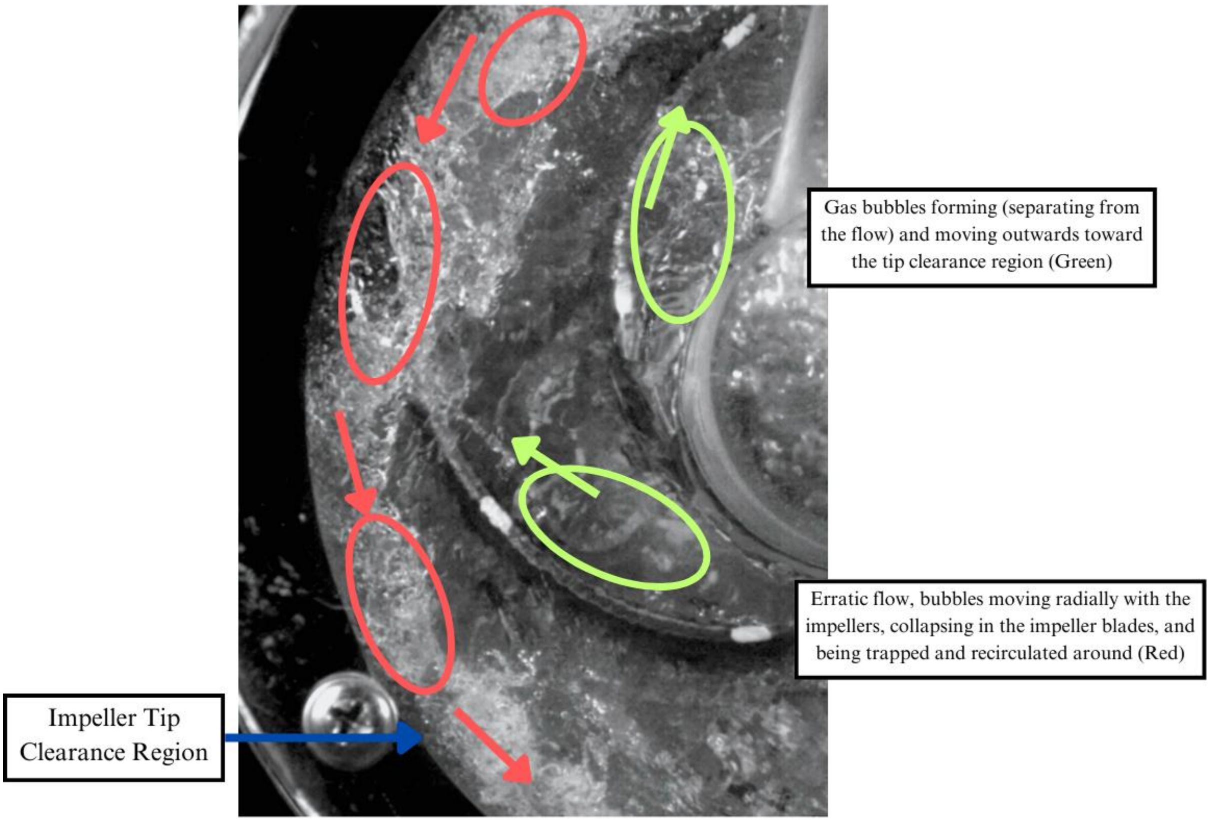

Fig. 19. Flow instability and gas accumulation at 1750 rpm, captured at ~0:40s

Additionally, Figure 20, taken from high-speed footage at 750 rpm (3.73k fps), illustrates another aspect of flow instability. The captured image shows gas clustering and intermittent phase collapse, where gas pockets momentarily shrink or disappear due to sudden pressure recovery and turbulent mixing. This matches the CFD predictions in Figure 14(a) and (b) which suggested that at high GVFs, localized phase separation could lead to transient gas pocket breakdown.

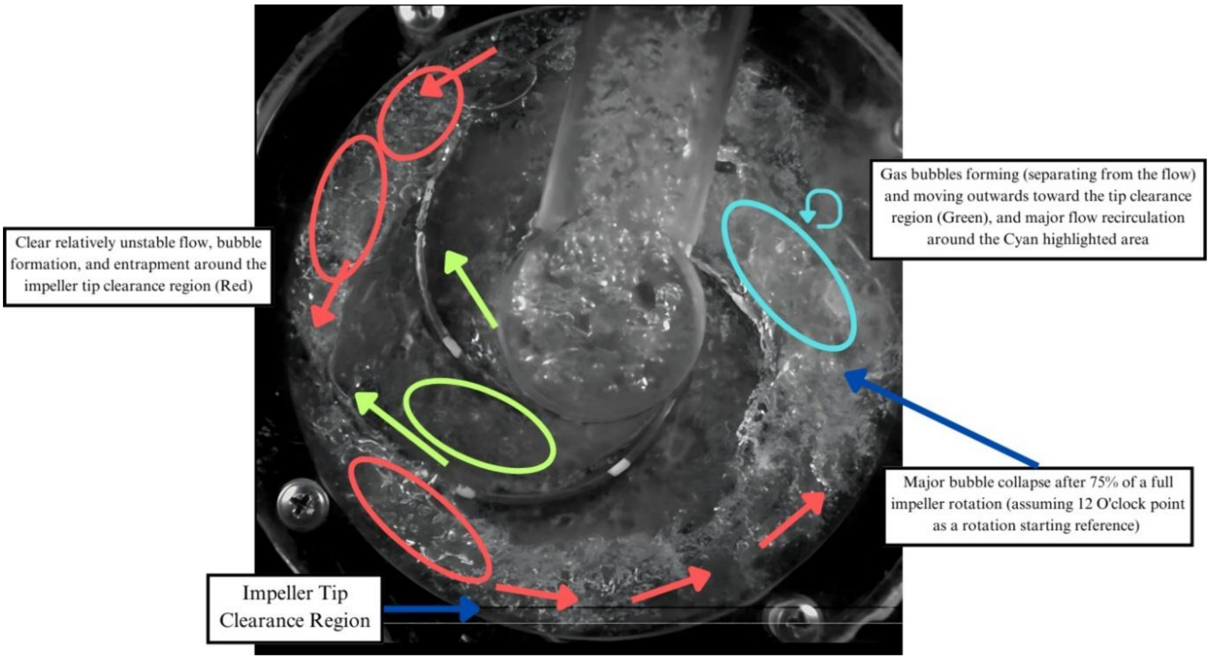

Fig. 20. Flow instability and gas collapse at 750 rpm, captured in 3.73k fps footage

3.3 Comparison of Simulation and Experimental Observations

The numerical and experimental results exhibit several key similarities, reinforcing the validity of the CFD models while also revealing some differences due to real-world complexities. The following discussion highlights the major agreements, discrepancies and their implications for ESP performance.

3.3.1 Gas distribution and phase separation trends

Both CFD and high-speed camera footage confirm that gas entrainment follows the primary liquid streamlines at low GVFs, with gradual separation occurring at higher gas concentrations. The simulations in Figure 8 and Figure 9 predict that gas tends to accumulate near the blade trailing edges and diffuser region, which was experimentally observed in Figure 17(a) and (b). The high-speed footage captures bubbles following impeller flow paths before concentrating near the tip clearance, validating the numerical predictions of phase separation zones.

3.3.2 Gas retention and tip clearance effects

The simulation results (Figure 11 and Figure 12) indicate that gas retention increases significantly as tip clearance widens, leading to localized pockets of stagnant gas. The high-speed camera images in Figure 18 confirm this phenomenon, where bubbles are observed accumulating in the clearance region instead of being expelled efficiently. This consistency between numerical and experimental results highlights the importance of clearance geometry in determining gas-handling capability.

3.3.3 Flow instabilities and recirculation zones

The CFD-predicted recirculation zones (Figures 10 and 13(b)) match well with experimental footage at 750 rpm and 1750 rpm (Figure 17(a), (b) and 19). Both methods show that higher GVFs promote gas trapping within the impeller and diffuser passages, leading to unsteady flow behaviour and bubble recirculation. This agreement suggests that CFD effectively captures the primary flow instability mechanisms affecting ESP performance under multiphase conditions.

3.3.4 Discrepancies between CFD and experimental results

One key difference arises in the trajectory of individual gas bubbles. While simulations assume continuous gas-phase transport along numerical streamlines, the high-speed camera footage reveals that bubbles exhibit more chaotic, intermittent movement. This is particularly evident in Figure 17a, 17b, where experimental observations suggest that small bubbles frequently break away from the main flow paths, whereas the CFD models predict a smoother gas motion pattern. This discrepancy may be attributed to:

i. CFD’s limitation in capturing fine-scale turbulence effects influencing individual bubble paths.
ii. Unresolved transient forces in the numerical model, leading to over-simplified gas motion predictions.

Experimental footage at 750 rpm and 1750 rpm (Figure 19 and Figure 20) shows sudden bubble collapse and reformation, likely due to local pressure recovery effects. In contrast, the numerical results (Figure 14(a) and (b)) predict a more gradual transition in phase separation without capturing these abrupt gas disappearance and reappearance events. This discrepancy suggests that:

i. The numerical model may be underestimating compressibility and pressure fluctuations, leading to an overly steady-state gas distribution.
ii. Cavitation-like effects in real experiments could be influencing bubble collapse, which is not explicitly modelled in CFD.
iii. While the CFD results predict a nonlinear decrease in head rise with increasing GVF (Figure 7), the experimental results suggest an even more pronounced performance drop beyond a critical threshold. This suggests that:
iv. The numerical model may slightly overestimate the ESP’s gas-handling capability, possibly due to idealized turbulence modelling.

Unexpected experimental losses (e.g., gas coalescence leading to increased drag) could contribute to the more severe performance decline observed in real conditions.

4. Conclusions

This study provides a comprehensive evaluation of multiphase flow behaviour in Electric Submersible Pumps (ESPs) by integrating Computational Fluid Dynamics (CFD) simulations with high-speed camera experiments. The findings offer valuable insights into the gas-handling limitations of ESPs, highlighting the effects of gas volume fraction (GVF) and impeller tip clearance on flow behaviour and performance degradation.

The results demonstrate that at low GVFs, gas is well-distributed within the liquid phase, following the impeller-induced streamlines without significant disruption to the continuous flow. However, as GVF increases, gas begins to accumulate in low-pressure regions, particularly near the impeller tip clearance and diffuser vanes, forming recirculating gas pockets. These retention zones create localized flow instabilities, reducing effective energy transfer and contributing to performance degradation. Both CFD and experimental results confirm that increasing tip clearance exacerbates gas retention, allowing stagnant gas layers to form within the impeller passages. This results in higher hydraulic losses, particularly at high GVFs, where the formation of continuous gas structures disrupts normal liquid flow. The high-speed camera images capture bubble clustering near the impeller tip clearance, mirroring the gas accumulation regions predicted by CFD. This agreement reinforces the importance of optimizing tip clearance to mitigate gas entrapment effects.

However, discrepancies arise in the transient behaviour of gas bubbles. While the CFD models accurately predict bulk gas distribution trends and phase separation zones, the high-speed camera footage reveals intermittent gas collapse and chaotic bubble motion, which are not fully captured in the numerical results. These differences suggest that CFD models may underpredict fine-scale turbulence effects and localized pressure fluctuations, particularly under high-GVF conditions. The experimental results also indicate a more severe drop in head rise beyond a critical GVF, suggesting that numerical models may slightly overestimate the ESP's gas-handling capability due to idealized turbulence assumptions. The findings of this study emphasize the need for refined CFD approaches to improve gas-liquid interaction modelling, particularly in areas such as bubble breakup, turbulence-driven motion and transient gas collapse phenomena. Future work should explore advanced turbulence models and compressibility effects to enhance the accuracy of CFD predictions in multiphase conditions. Additionally, experimental validation at higher rotational speeds and varying tip clearance configurations could provide further insights into optimizing ESP designs for gas-laden environments.

Overall, this research enhances the understanding of gas retention, phase separation and flow instabilities in ESPs, offering practical guidance for improving pump performance and reliability in multiphase flow applications. The results serve as a foundation for developing enhanced ESP designs with improved gas-handling efficiency, ensuring more stable operation in oil and gas, mining and other fluid transportation industries.

Acknowledgement
This research was not funded by any grant.

References

[1] Bremner, Chad, Grant Harris, Alex Kosmala, Barry Nicholson, A. Ollre, M. Pearcy, C. Salmas, and S. Solanki. "Evolving technologies: electrical submersible pumps." *Oilfield Rev* 18, no. 4 (2006): 30-43.

[2] Khalaji, Reza, and Mohsen Jannati. "SCADA-Based Protection of Centrifugal and Submersible Electric Pumps in the Water Industry." *Journal of Water and Wastewater Science and Engineering* 7, no. 1 (2022): 62-76.

[3] Nave, Michael L. "Considerations for application of electrical submersible pumps for underground coal mine dewatering." In *Conference Record of the 1988 IEEE Industry Applications Society Annual Meeting*, pp. 1263-1266. IEEE, 1988. https://doi.org/10.1109/IAS.1988.25223

[4] Çalisir, Sedat. "The evaluation of performance and energy usage in submersible deep well irrigation pumping plants." *Agricultural Mechanization in Asia Africa And Latin America* 38, no. 1 (2007): 9.

[5] Zhang, Wei-xian. "Nanoscale iron particles for environmental remediation: an overview." *Journal of nanoparticle Research* 5 (2003): 323-332. https://doi.org/10.1023/A:1025520116015

[6] Shahid, Salman, Abdul Qader Hassan, Sharul Sham Dol, Mohamed S. Gadala, and Mohd Shiraz Aris. "Effects of gas volume fractions on electrical submersible pump performance under two-phase flow." *Platform: A Journal of Engineering* 5, no. 2 (2021): 2-9. https://doi.org/10.61762/pajevol5iss2art12255

[7] Shahid, Salman, Sharul Sham Dol, Abdul Qader Hasan, Omar Mustafa Kassem, Mohamed S. Gadala, and Mohd Shiraz Aris. "A review on electrical submersible pump head losses and methods to analyze two-phase performance curve." *WSEAS Transactions on Fluid Mechanics* 16 (2021): 14-31. https://doi.org/10.37394/232013.2021.16.3

[8] Hasan, Abdulqader, UNITED ARAB EMIRATES, MOHAMED S. GADALA, SALMAN SHAHID, Mohd Shiraz Aris, SHARUL SHAM DOL, and MOHAMMED ALAVI. "Numerical investigation of wall shear stress under single-phase and two-phase flow in the electrical submersible pump." *WSEAS Transactions on Fluid Mechanics* 16 (2021): 158-167. https://doi.org/10.37394/232013.2021.16.15

[9] Shahid, Salman, Abdul Qader Hasan, Sharul Sham Dol, Mohamed S. Gadala, and Mohd Shiraz Aris. "Effects of near-wall vortices on wall shear stress in a centrifugal pump impeller." *WSEAS Transactions on Fluid Mechanics* 16 (2021): 37-47. https://doi.org/10.37394/232013.2021.16.5

[10] Pervaiz, Salman Shahid, Abdulqader Hasan, Sharul Sham Dol, and Mohamed S. Gadala. "Numerical investigation of turbulence production under two-phase flow in a simulation of electrical submersible pump performance." *ASME Open Journal of Engineering* 1 (2022). https://doi.org/10.1115/1.4054034

[11] Morrison, Gerald, S. Pirouspanah, K. Kirland, Stuart L. Scott, and Lissett J. Barrios. "Performance evaluation of a multiphase electric submersible pump." In *Offshore Technology Conference*, p. D031S031R002. OTC, 2014. https://doi.org/10.4043/25080-MS

[12] Pessoa, Rui, and Mauricio Prado. "Experimental investigation of two-phase flow performance of electrical submersible pump stages." In *SPE Annual Technical Conference and Exhibition?*, pp. SPE-71552. SPE, 2001. https://doi.org/10.2118/71552-MS

[13] Zhou, Desheng, and Rajesh Sachdeva. "Simple model of electric submersible pump in gassy well." *Journal of Petroleum Science and Engineering* 70, no. 3-4 (2010): 204-213. https://doi.org/10.1016/j.petrol.2009.11.012

[14] Bagci, A. Suat, Murat Kece, and Jocsiris Nava. "Challenges of using electrical submersible pump (ESP) in high free gas applications." In *SPE International Oil and Gas Conference and Exhibition in China*, pp. SPE-131760. SPE, 2010. https://doi.org/10.2118/131760-MS

[15] Ahmad, Aida Husna, Abu Bakar, Anis Farhana & Osman, Shahrul Azmir. “CFD Analysis of Thermal Conditions and Airflow Patterns in Commercial Laundry Facility using ANSYS Fluent Simulation.” *Journal of Advanced Research in Fluid Mechanics and Thermal Sciences*, 126(2), (2025): 106–126. https://doi.org/10.37934/arfmts.126.2.106126

[16] Rahayu, Nur Indri, Muktiarni and Ismail, Affero. “An Analysis of Computational Fluid Dynamics in Sports Performance of Professional Sport.” *CFD Letters*, 17(7), (2025): 206–215. https://doi.org/10.37934/cfdl.17.7.206215

[17] Hasan, Wajeeh K., Hussein, Mohammed Ali Mahmood and Saieed, Ali Najim Abdullah. “Enhancing Heat Transfer Performance in Heat Exchangers using Nanoparticle-Infused Fluids: A Computational Approach.” *CFD Letters*, 17(7), (2025): 32–46. https://doi.org/10.37934/cfdl.17.7.3246

[18] Perissinotto, Rodolfo Marcilli, William Monte Verde, Jorge Luiz Biazussi, Marcelo Souza de Castro, and Antonio Carlos Bannwart. "Experimental Analysis on the Velocity of Oil Drops in Oil–Water Two-Phase Flows in Electrical Submersible Pump Impellers." *Journal of offshore mechanics and arctic engineering* 141, no. 4 (2019): 041301. https://doi.org/10.1115/1.4042000

[19] Bulgarelli, Natan Augusto Vieira, Jorge Luiz Biazussi, William Monte Verde, Carlos Eduardo Perles, Marcelo Souza de Castro, and Antonio Carlos Bannwart. "Experimental investigation on the performance of Electrical Submersible Pump (ESP) operating with unstable water/oil emulsions." *Journal of Petroleum Science and Engineering* 197 (2021): 107900. https://doi.org/10.1016/j.petrol.2020.107900

[20] Yang, Yang, Xionghuan Chen, Ling Bai, Yulong Yao, Hui Wang, Leilei Ji, Zhaoming He, Xiangyu Song, and Ling Zhou. "Quantification and investigation of pressure fluctuation intensity in a multistage electric submersible pump." *Physics of Fluids* 35, no. 3 (2023). https://doi.org/10.1063/5.0136664

[21] Marie-Magdeleine, Artem, R. Fortes-Patella, Nicolas Lemoine, and Nicolas Marchand. "Application of unsteady flow rate evaluations to identify the dynamic transfer function of a cavitatingVenturi." In *IOP Conference Series: Earth and Environmental Science*, vol. 15, no. 6, p. 062021. IOP Publishing, 2012. https://doi.org/10.1088/1755-1315/15/6/062021

[22] Hussein, Mennatallah. "Reduced Order Modeling of a Rocket Engine Turbopump Inducer for Assessment of Pogo Instability." PhD diss., Massachusetts Institute of Technology, 2023.

[23] Patil, Abhay, Shyam Sundar, Adolfo Delgado, and Jose Gamboa. "CFD based evaluation of conventional electrical submersible pump for high-speed application." *Journal of Petroleum Science and Engineering* 182 (2019): 106287. https://doi.org/10.1016/j.petrol.2019.106287

[24] Parikh, Trupen, Michael Mansour, and Dominique Thévenin. "Investigations on the effect of tip clearance gap and inducer on the transport of air-water two-phase flow by centrifugal pumps." *Chemical Engineering Science* 218 (2020): 115554. https://doi.org/10.1016/j.ces.2020.115554

[25] Mansour, Michael, Bernd Wunderlich, and Dominique Thévenin. "Effect of tip clearance gap and inducer on the transport of two-phase air-water flows by centrifugal pumps." *Experimental Thermal and Fluid Science* 99 (2018): 487-509. https://doi.org/10.1016/j.expthermflusci.2018.08.018

[26] Zhu, Jianjun, and Hong-Quan Zhang. "A review of experiments and modeling of gas-liquid flow in electrical submersible pumps." *Energies* 11, no. 1 (2018): 180. https://doi.org/10.3390/en11010180

[27] Garvin, Justin W. *A student's guide to the Navier-Stokes equations*. Cambridge University Press, 2023. https://doi.org/10.1017/9781009236119

[28] Könözsy, László. "The k-ω shear-stress transport (SST) turbulence model." In *A new hypothesis on the anisotropic reynolds stress tensor for turbulent flows: volume i: theoretical background and development of an anisotropic hybrid k-omega shear-stress transport/stochastic turbulence model*, pp. 57-66. Cham: Springer International Publishing, 2019. https://doi.org/10.1007/978-3-030-13543-0_3
[29] Hirt, Cyril W., and Billy D. Nichols. "Volume of fluid (VOF) method for the dynamics of free boundaries." *Journal of computational physics* 39, no. 1 (1981): 201-225. https://doi.org/10.1016/0021-9991(81)90145-5
[30] Manninen, Mikko, Veikko Taivassalo, and Sirpa Kallio. "On the mixture model for multiphase flow." (1996).
[31] Shynybayeva, Amina, and Luis R. Rojas-Solórzano. "Eulerian–Eulerian modeling of multiphase flow in horizontal annuli: Current limitations and challenges." *Processes* 8, no. 11 (2020): 1426. https://doi.org/10.3390/pr8111426